



## Research article

# Reprogramming magnetic anisotropy: Field-assisted annealing of Fe-based bulk metallic glass ribbons

Priyanka Saha <sup>a</sup>, Julia Löfstrand <sup>a</sup>, Fernando Maccari <sup>b</sup>, Franziska Scheibel <sup>b</sup>,  
Oliver Gutfleisch <sup>b</sup>, Martin Sahlberg <sup>c</sup>, Petra E. Jönsson <sup>a</sup>\*

<sup>a</sup> Uppsala University, Department of Physics and Astronomy, Materials Physics, Box 516, SE 751 37, Uppsala, Sweden

<sup>b</sup> Technical University of Darmstadt, Department of Functional Materials, Institute of Material Science, Peter-Grünberg-Str. 16, Darmstadt, 64287, Germany

<sup>c</sup> Uppsala University, Department of Chemistry, Box 538, SE 751 21, Uppsala, Sweden



## ARTICLE INFO

## Keywords:

Magnetic field annealing  
Magnetic domain imaging  
Kerr microscopy  
Nanocrystallization  
Bulk metallic glasses

## ABSTRACT

Fe-based bulk metallic glasses (BMGs) are recognized for their excellent soft magnetic properties, further tunable through thermal processing. In this study, we investigate the effects of zero-field and field-assisted annealing on crystallization and stress-driven magnetic properties of  $\text{Fe}_{80}\text{B}_{12}\text{P}_4\text{Si}_{2.7}\text{C}_{1.3}$  melt-spun ribbons. Using Kerr microscopy and magnetic measurements, we analyze the evolution of magnetic domains, anisotropy, and stress relaxation under different annealing conditions. Our results reveal that magnetic-field-assisted annealing below the Curie temperature effectively suppresses crystallization while reprogramming magnetic anisotropy, leading to improved soft magnetic properties. Reprogramming the magnetic anisotropy by annealing in a longitudinal magnetic field of 16 kA/m is effective only when the system remains fully amorphous. In a partially crystallized system, local anisotropy dominates over field-induced anisotropy. These findings clarify the thermal and structural conditions required for controlled tuning of magnetic anisotropy and soft magnetic performance, providing deeper insight into the interplay between stress, crystallization, and magnetic anisotropy in Fe-based BMGs.

## 1. Introduction

The urgent need to realize the green transition through electrification necessitates developing lightweight, miniaturized, and energy-efficient magnetic functional devices. Fe-rich amorphous alloys with excellent soft magnetic properties (SMPs), such as high magnetic saturation flux density ( $B_S$ ), low coercivity ( $H_C$ ), and low core loss, have great potential for application in e.g. high-efficiency transformers and electric machines [1–3].

Widely used Fe-based amorphous alloys, such as Metglas (Fe-Si-B-type alloys), produced in the form of ribbon using rapid solidification via the melt spinning process, exhibit lower hysteresis loss but also a lower  $B_S$  compared to silicon steel. The enhancement of  $B_S$  to the value of Fe-Si steel has been the major driving force in the search for alternative alloys. Great efforts have been devoted to increasing  $B_S$  by modifying alloy compositions [4,5], post-processing heat treatment [6–8], and nanocrystallization [3,9]. The design of novel Fe-based amorphous alloys, by increasing Fe content and adjusting metalloid elements, is a trade-off between high  $B_S$  and the amorphous-forming ability (AFA) [10].

Fe-Si-B-C series of amorphous alloys exhibit high  $B_S$  but suffer from low AFA [5]. Wang et al. showed that combining P in the system helps to improve  $B_S$  and AFA [11]. However, P-containing amorphous alloys are prone to surface crystallization [12]. Surface crystallization of amorphous ribbons has been studied thoroughly over the years, and researchers pointed out the following reasons for the surface crystallization to occur: (i) preferred oxidation on the surface which triggers the crystallization, (ii) depletion of metalloids in the surface region [12–14], and (iii) lower cooling rate on the air side of the ribbon compared to the wheel side [15]. Lopatina et al. emphasized that optimizing quenching conditions is critical to minimize surface crystallization in P-containing alloys [13]. Meanwhile, nanocrystallization has been explored as a means of enhancing  $B_S$ , although it often introduces processing challenges [16]. Researchers have demonstrated rapid thermal annealing as an effective approach to improve SMPs by controlling nanograin size [3,17].

Magnetic field-assisted annealing also proved effective in improving the magnetic softness in both amorphous and nanocrystalline alloys [18]. This technique induces uniaxial magnetic anisotropy along

\* Corresponding author.

E-mail address: [petra.jonsson@physics.uu.se](mailto:petra.jonsson@physics.uu.se) (P.E. Jönsson).

<https://doi.org/10.1016/j.jalcom.2025.183153>

Received 13 May 2025; Received in revised form 31 July 2025; Accepted 19 August 2025

Available online 26 August 2025

0925-8388/© 2025 The Authors. Published by Elsevier B.V. This is an open access article under the CC BY license (<http://creativecommons.org/licenses/by/4.0/>).

the applied field direction and reduces core loss through domain refinement [19–21]. The annealing of amorphous alloys ( $\text{Fe}_{80}\text{Si}_9\text{B}_{11}$ ) below the crystallization temperature in the presence of a magnetic field of 1 T improved SMPs due to the formation of densely packed clusters of spherical symmetry, as reported by Wang et al. [22]. Li et al. [7] reported that magnetic field-assisted annealing improved the SMPs of  $\text{Fe}_{83.3}\text{Si}_{11.2}\text{P}_{2.7}\text{C}_{0.8}$  amorphous alloys. However, Miglierini et al. showed that the presence of a magnetic field of 0.652 T accelerates the crystallization process in comparison to isothermal annealing performed at the same temperature under zero field conditions in  $\text{Fe}_{90}\text{Zr}_7\text{B}_3$  alloys [23]. These studies suggest that magnetic-field assisted annealing can improve the SMPs by magnetic softening or can lead to crystallization, and the annealing time ( $t_a$ ) should also be taken into account to gain a proper understanding of the magnetic field annealing and crystallization process of Fe-rich BMGs. Amorphous alloys with large temperature intervals between  $T_C$  and  $T_{X1}$ , where  $T_{X1}$  is the first crystallization temperature, result in better structural homogeneity and SMPs during the annealing process [7]. Moreover, in superior glass-forming alloys, atomic mobility remains relatively slow even above the glass transition temperature ( $T_g$ ), which effectively suppresses structural rearrangements and delays crystallization. This sluggish dynamic behavior contributes to their excellent thermal stability and enables a wider processing window, critical to achieving and maintaining the amorphous structure [24]. A comprehensive literature review suggests that in magnetic field annealing, it is important to consider  $T_C$ ,  $T_{X1}$ ,  $T_g$ , and  $t_a$  along with  $T_a$ . However, while field-assisted annealing can influence crystallization kinetics, most studies have focused on  $T_a$  and magnetic field strength, with relatively little attention given to the role of annealing time. The presence of phosphorus further complicates the dependency between the magnetic field intensity and  $T_a$  by altering the crystallization dynamics, yet its effects on domain formation remain poorly understood. This led us to explore the effects of magnetic field-assisted annealing on the stress-driven magnetic properties of Fe-rich P-containing BMGs with various annealing conditions by modifying the field orientation,  $T_a$ , and  $t_a$ . The presence of phosphorus mandates a deeper understanding of SMPs in relation to surface crystallization and stress in the system.

Here, we investigate the impact of zero field and field-assisted annealing on melt-spun ribbons of composition  $\text{Fe}_{80}\text{B}_{12}\text{P}_4\text{Si}_{2.7}\text{C}_{1.3}$ , focusing on the evolution of magnetic domain, stress relaxation, and crystallization behavior. Using Kerr microscopy and magnetic measurements, we elucidate the interplay between annealing conditions and crystallization, revealing how field-induced and crystallization-induced anisotropies influence domain structures and magnetic properties. This study establishes strategies for reprogramming the magnetic anisotropy by field-annealing below  $T_C$ , providing new insight into stress-driven magnetic properties and advancing the design of Fe-based BMGs for soft magnetic applications.

## 2. Methodologies

Alloy ingots with composition  $\text{Fe}_{80}\text{B}_{12}\text{P}_4\text{Si}_{2.7}\text{C}_{1.3}$  were prepared by arc melting a mixture of Fe (99.95%), B (> 98%) in FeB form obtained from Höganäs AB, P in  $\text{Fe}_2\text{P}$  form, Si (99.999%) and C (99.98%) in an Argon atmosphere.  $\text{Fe}_2\text{P}$  was synthesized in the laboratory using an induction melting process with pure P (99.99%) and Fe (99.95%). The alloy ingots were quenched into ribbons in a single-roller melt spinning method, resulting in as-quenched (AQ) ribbons with a width of 2 mm and a thickness of 12–15  $\mu\text{m}$ , respectively. The AQ ribbons were subsequently heat-treated under continuous Ar flow in a custom-built furnace equipped with a PID temperature controller. Heat treatments were performed at a controlled heating rate of 5  $^\circ\text{C}/\text{min}$ , followed by furnace cooling, at different temperatures ranging between 350  $^\circ\text{C}$ –500  $^\circ\text{C}$  by varying the annealing times ( $t_a$ ) and under three conditions: (1) without a magnetic field, (2) in the presence of a longitudinal magnetic field (LFA), and (3) in the presence of a transverse magnetic field

(TFA). For the magnetic field-assisted annealing, a high-temperature AlNiCo magnet was employed, producing a magnetic field of 16 kA/m.

The structural properties were characterized on both the air and wheel sides of the ribbons by incorporating a Bruker D8 advanced powder X-ray diffractometer with Cu-K $\alpha$  source and a Netzsch DSC 440 F1 Pegasus differential scanning calorimeter (DSC) with a heating rate of 10  $^\circ\text{C}/\text{min}$  equipped with a Pt furnace and  $\text{Al}_2\text{O}_3$  crucible. The DSC analysis provided information on the glass transition temperature, Curie temperature, and crystallization temperatures, which were used to determine the appropriate annealing temperature range. Magnetic measurements were performed on a 2 mm  $\times$  2 mm piece (cut from both AQ and heat-treated ribbons) using a Lakeshore 7407 vibrating sample magnetometer (VSM). For the VSM measurements, the magnetic field was applied in the ribbon plane along the length of the ribbon for all the samples. The magnetic domains of the samples were imaged in an Evico magnets MOKE microscope with a 20X objective lens and an applied field aligned along the ribbon axis. The air side of the melt-spun ribbon, which is smoother compared to the wheel side, was used to image the magnetic domains without any surface treatment. A 1.5 cm long ribbon piece was mapped in the MOKE microscope to average the magnetic domain data for each sample, including both AQ and heat-treated ribbons. Magnetic susceptibility measurements were performed on the ribbons with an MFK1-FA susceptibility bridge (Agico Inc.) with an applied ac field of 200 A/m and a frequency of 976 Hz. The measurements were carried out over a temperature range from room temperature to 700  $^\circ\text{C}$ , with a heating rate of 10  $^\circ\text{C}/\text{min}$ .

## 3. Results and discussion

Fig. 1(a) presents the room-temperature magnetization ( $M$ - $H$ ) loops of the as-quenched (AQ) ribbons and those subjected to the highest annealing temperature ( $T_a = 480$   $^\circ\text{C}$ ) for  $t_a = 20$  min. The inset of Fig. 1(a) provides an enlarged view of the central region for a detailed examination of the coercivity ( $H_C$ ), highlighting the excellent soft magnetic properties (SMPs) of the AQ ribbons. As shown in the  $H_C$  vs. annealing temperature ( $T_a$ ) plot, in Fig. 1(b),  $H_C$  decreases with an increase in  $T_a$  as a result of structural relaxation and stress release, reaching a minimum at 390  $^\circ\text{C}$ . At  $T_a = 400$   $^\circ\text{C}$ , magnetic hardening is observed, followed by a softening trend as  $T_a$  increases to 435  $^\circ\text{C}$ , after which  $H_C$  increases again at higher  $T_a$ . The saturation magnetization ( $M_S$ ) of the annealed ribbons remains consistent with that of the AQ ribbons within the temperature range of 350  $^\circ\text{C}$  to 450  $^\circ\text{C}$ , with a value of  $172 \pm 9$  emu/g.  $M_S$  of the ribbons annealed at 480  $^\circ\text{C}$  enhances to  $184 \pm 10$  emu/g. For annealed ribbons in the presence of a magnetic field, a lower  $H_C$  is obtained at  $T_a = 400$   $^\circ\text{C}$ . A detailed discussion of the effects of magnetic field annealing on the SMPs is presented later.

The amorphous nature of the AQ ribbons is verified by the X-ray diffraction (XRD) pattern in Fig. 2. The enhanced  $M_S$  and  $H_C$  in the ribbons annealed at 480  $^\circ\text{C}$  for  $t_a = 20$  min is due to crystallization with prominent  $\alpha$ -Fe phase formation, as verified by the XRD pattern in Fig. 2. XRD data of the ribbon annealed at 500  $^\circ\text{C}$  are used to identify the crystalline phases formed, and are correlated with those in the ribbon annealed at 480  $^\circ\text{C}$ . XRD files with matched peak positions and identified phases are shown in Figures S1 and S2 of the supplementary material information. We observe only the amorphous hump up to  $T_a = 435$   $^\circ\text{C}$ . The annealed ribbons, treated in the temperature range of 350  $^\circ\text{C}$  to 480  $^\circ\text{C}$ , displaying significant changes in the magnetic properties in comparison to the AQ ribbons, are chosen to be included in Fig. 2 and the rest are represented in Figure S3 of the supplementary material information. The differential scanning calorimetry (DSC) curve, measured with a heating rate of 10  $^\circ\text{C}/\text{min}$ , in Fig. 3 shows the glassy amorphous nature of the AQ ribbons, with a glass transition temperature  $T_g = 440$   $^\circ\text{C}$  and a first crystallization onset temperature  $T_{X1} = 490$   $^\circ\text{C}$ . The wide temperature interval between  $T_g$  and  $T_{X1}$  suggests a good glass forming ability of the alloy system, which is crucial for structural relaxation and stress release, inhibiting

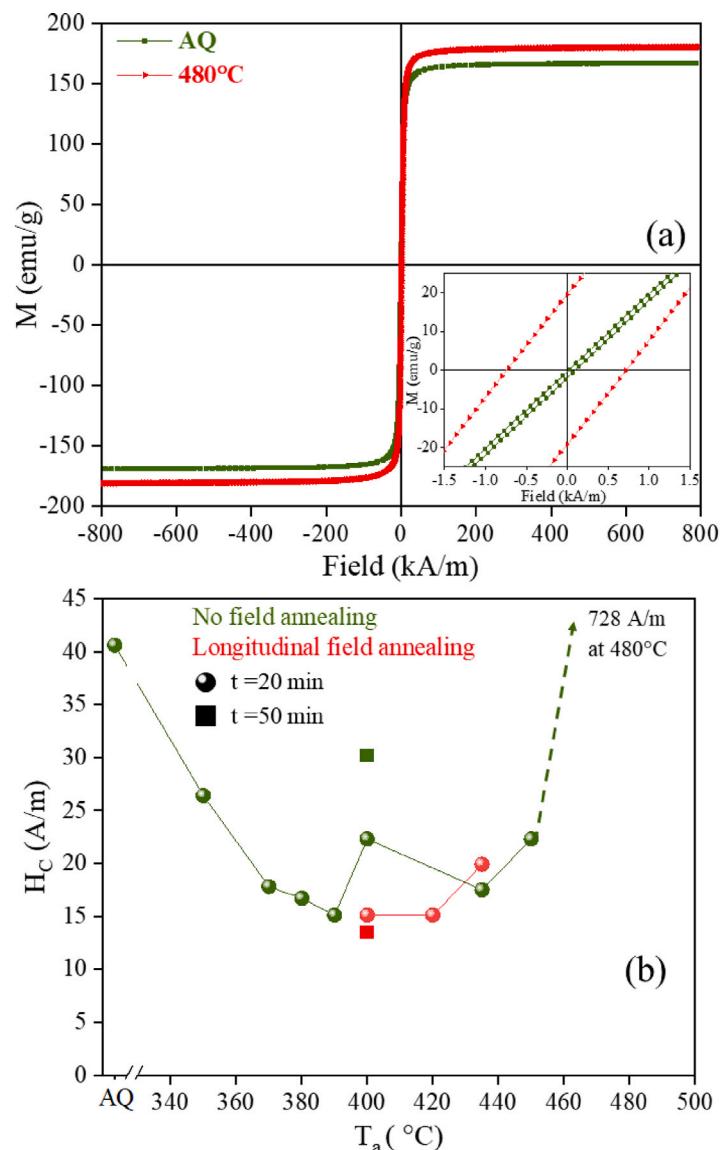


**Fig. 1.** (a) The room-temperature magnetization ( $M$ - $H$ ) loops of an AQ ribbon and a ribbon annealed at 480 °C for  $t_a = 20$  min with an enlarged version in the inset. (b) Variation of  $H_C$  with annealing temperature  $T_a$  under different annealing time ( $t_a = 20$  min and 50 min) and annealing conditions, such as in absence of a magnetic field and the presence of a longitudinal magnetic field.

crystallization during annealing. The small hump in the DSC curve near 400 °C indicates that the ferromagnetic Curie temperature ( $T_C$ ) of the AQ sample is approximately around that temperature.

To understand the magnetic behavior of the AQ and the annealed ribbons for  $t_a = 20$  min, the surface magnetic domains are imaged after annealing, as shown in Fig. 4. Kerr images were collected in two modes: pure longitudinal mode, indicated by vertical arrows, and pure transverse mode, indicated by horizontal arrows, as shown in Fig. 4. The magnetic anisotropy direction can be deduced from the orientation of the domain in the images. The Kerr sensitivity was selected based on the micrograph that provided the best contrast while imaging the surface domains. All the images are collected with the same microscope settings, and depending on the magnetic anisotropy alignment along the ribbon axis or the ribbon width, the Kerr sensitivity is adjusted to the longitudinal or transverse modes, respectively. The labyrinth-like domain structure in the AQ ribbon (Fig. 4(a)) is a signature of stress-induced perpendicular anisotropy in the amorphous system [25]. With an increase in  $T_a$  the maze-like domains slowly vanish, as shown in Fig. 4 (b-d) and result in a homogeneous broad

domain arrangement with a 180 ° domain walls (Fig. 4(e)) at  $T_a = 390$  °C. As shown in Fig. 1(b), 390 °C is also the temperature where  $H_C$  is minimum. 390 °C can be ascribed as the optimal temperature to obtain microstructural homogeneity with improved SMPs and wide magnetic domains by annealing [26]. Above this optimal  $T_a$ , the increase in  $H_C$  can be attributed to the formation of nanocrystals. In the early stages of crystallization, magnetic hardening is attributed to weak intergranular magnetic coupling due to the large fraction of the amorphous phase [27]. The MOKE micrographs of the ribbons annealed at 400 °C show a narrow stripe domain alongside wide domains (marked in yellow in Fig. 4(f)), suggesting magnetic inhomogeneity within the amorphous matrix possibly due to crystallization or cluster formation [28]. However, the XRD pattern in Fig. 2 reveals the X-ray amorphous nature of the ribbon annealed at 400 °C, as evidenced by the presence of a broad hump without distinct crystalline peaks. This apparent contradiction suggests that at  $T_a = 400$  °C, the surface crystallization or nanocluster formation initiates and can be detected by analyzing surface domain patterns. Nanoclusters are a collection of atoms or small nanoparticles with some crystalline arrangement that

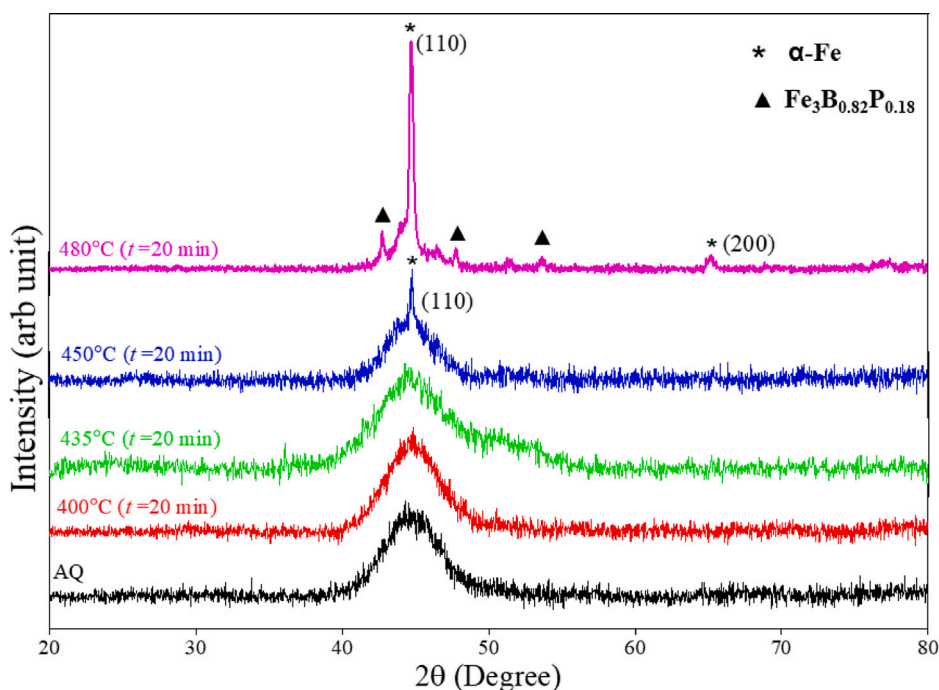


Fig. 2. XRD pattern of the AQ and annealed ribbons.

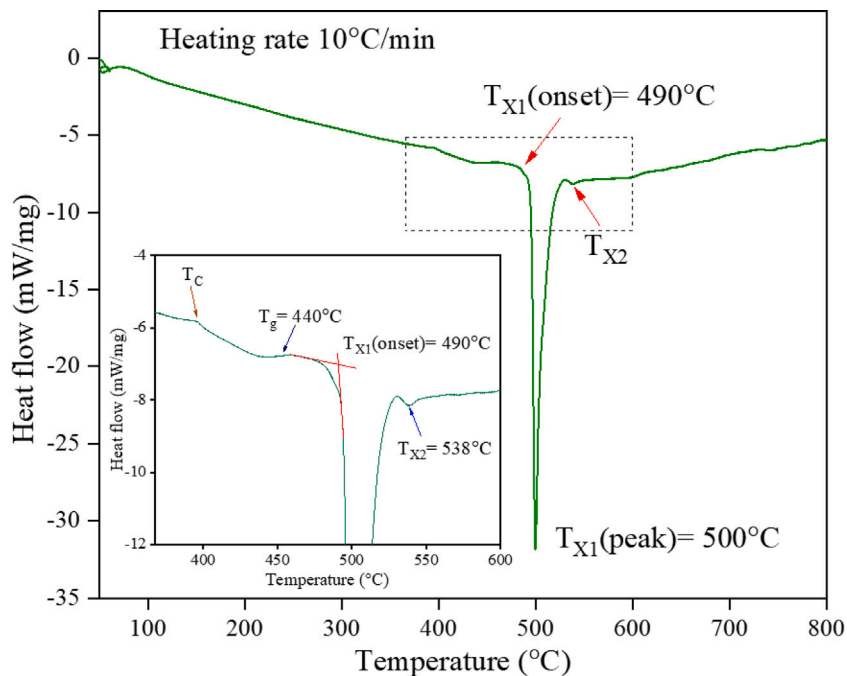


Fig. 3. DSC curve of the AQ ribbon. The inset figure shows the enlarged version of the dotted rectangular region for a better understanding of the transition temperatures.

are often difficult to detect using XRD due to the small size of the nanocrystals.

To have a better understanding of the domain patterns and domain evolution process in amorphous material linked to crystallization, the ribbons were annealed at higher temperatures to impose crystallization and visualize the associated stress signature via domain imaging. The crystallization onset temperature of the bcc-Fe phase is  $\sim 490^\circ\text{C}$ , as obtained from DSC analysis. The ribbons were annealed in the temperature range between  $400^\circ\text{C}$  to  $490^\circ\text{C}$ . The ribbons annealed at

$435^\circ\text{C}$  show reduced magnetic hardening compared to those annealed at  $400^\circ\text{C}$  (Fig. 1(b)). This is due to the formation of  $\alpha$ -Fe nanocrystals, which enhance the grain coupling between the nanocrystals, also observed in other amorphous and BMG systems [26,27]. As the XRD pattern (Fig. 2) of the ribbons annealed at  $435^\circ\text{C}$  does not show any prominent crystallization peak, the surface domains are imaged to detect the signatures of surface crystallization. Fig. 5(a) shows the domain pattern of the ribbons annealed at  $435^\circ\text{C}$ . The lower to the middle region of the measuring window exhibits domains with  $180^\circ$

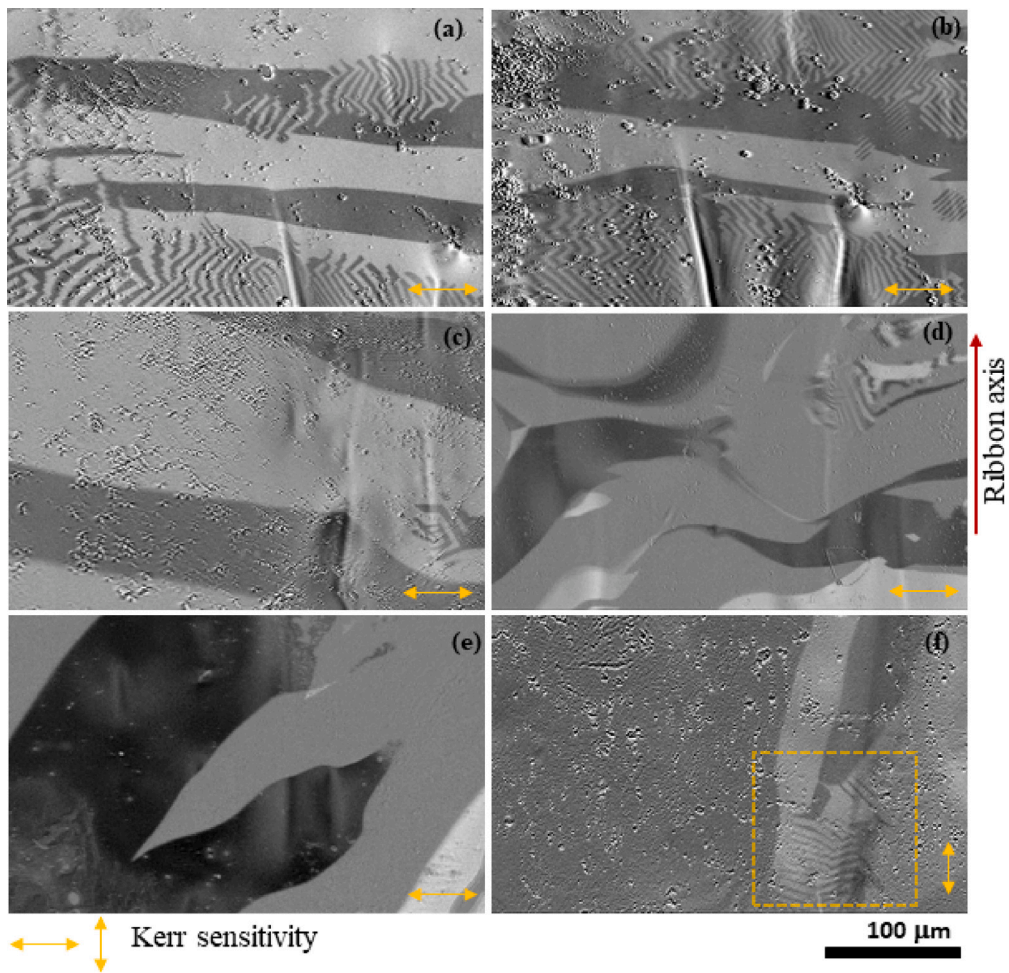


Fig. 4. Kerr micrographs of (a) a AQ ribbon and ribbons annealed at (b) 350 °C, (c) 370 °C, (d) 380 °C, (e) 390 °C, (f) 400 °C. All the ribbons are annealed for  $t_a = 20$  min. The Kerr sensitivity while collecting the domain images is indicated in the respective image. The yellow box in (f) shows the narrow stripe domain pattern after annealing at 400 °C.

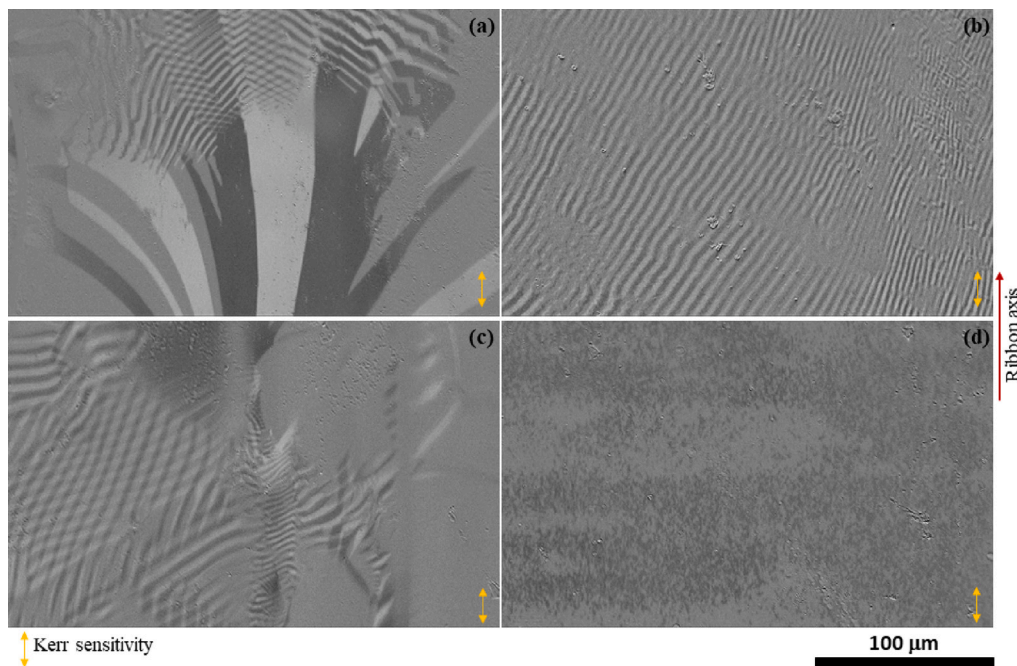
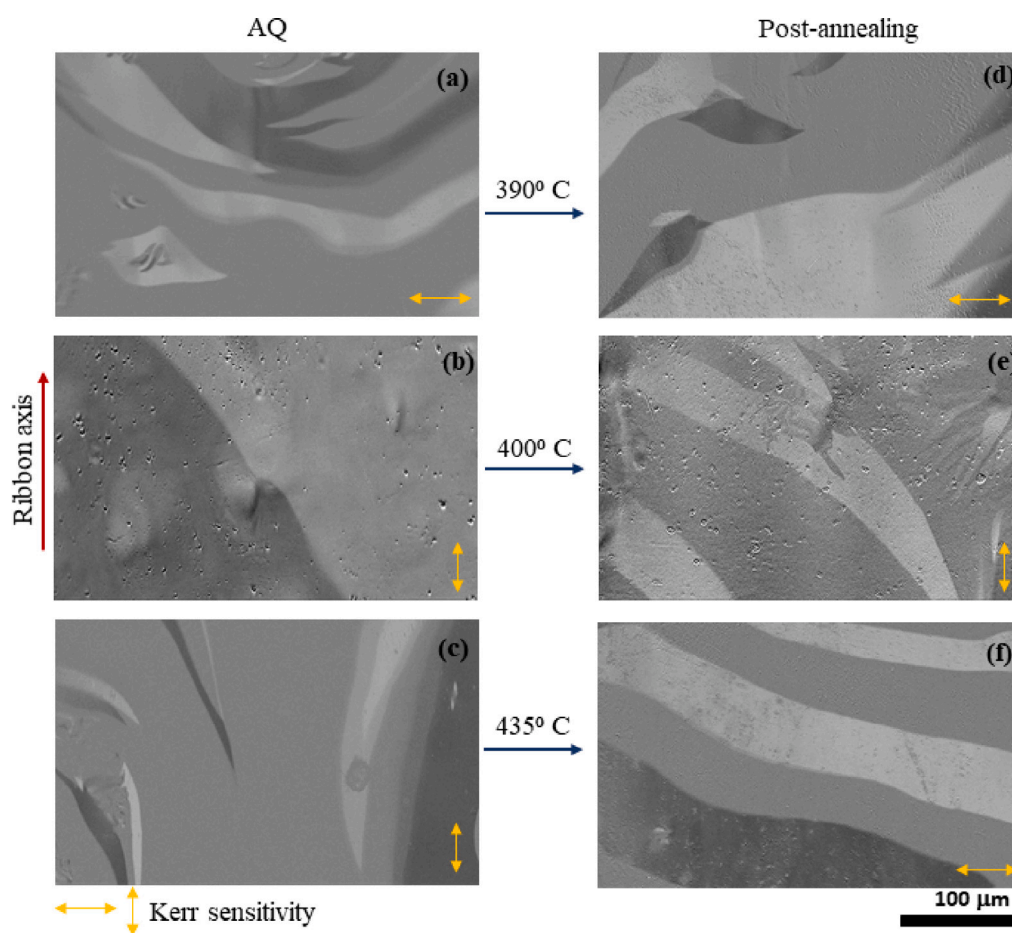


Fig. 5. Magnetic domain pattern of ribbons annealed at (a) 435 °C for  $t_a = 20$  min, (b) 450 °C for  $t_a = 20$  min, (c) 400 °C for  $t_a = 50$  min, and (d) 480 °C for  $t_a = 20$  min. All the images are collected in pure longitudinal mode, as shown in the respective images with vertical arrows.



**Fig. 6.** Magnetic domain patterns of the (a–c) AQ ribbons and ribbons annealed at (d) 390 °C, (e) 400 °C, (f) 435 °C for  $t_a = 20$  min. The same ribbon region was imaged before and after annealing for each annealing condition. The Kerr sensitivity while collecting the domain images is indicated in the respective image.

domain walls having magnetic anisotropy along the ribbon axis. In contrast, the upper region reveals a crisscross-domain pattern, indicating the possibility of surface crystallization. When  $T_a$  is increased to 450 °C with  $t_a = 20$  min, the XRD pattern shows  $\alpha$ -Fe crystallization peak on the amorphous hump, as observed in Fig. 2. From the Kerr micrograph of ribbons annealed at 450 °C, a combination of narrow stripe and maze-like domains is observed, as shown in Fig. 5(b). This observation suggests that in the presence of surface crystallization, narrow stripe-like magnetic domains are formed, reinforcing the claim of surface crystallization at 400 °C and 435 °C. The maze-like pattern observed in Fig. 5(b) results from the out-of-plane magnetic anisotropy that originated in the ribbons due to the surface crystallization-induced compressive stress [29].

Handling bulk metallic glassy ribbons often introduces mechanical stress, making them prone to surface defects such as cracks and pores, which significantly affect the surface magnetic domains. During annealing, atomic rearrangement in the amorphous ribbons can lead to embrittlement [16] and an increase in these surface imperfections. To confirm that the presence of narrow domains in the ribbons annealed at 400 °C is the effect of surface crystallization and not the result of mechanical stress, the AQ ribbon was subjected to a longer heat treatment for  $t_a = 50$  min at 400 °C, anticipating the growth of nanocrystalline grains. Magnetic measurements show that  $H_C$  increases to 30 A/m (for  $t_a = 50$  min) from 22 A/m (for  $t_a = 20$  min). After 50 min heat treatment, the magnetic domains exhibit narrow stripe domains and crisscross patterns, as shown in Fig. 5(c), confirming surface crystallization for  $t_a = 20$  min and further grain growth with prolonged annealing. The ribbons annealed at 480 °C result in sharp  $\alpha$ -Fe peaks, indicating full crystallization, showing no distinct magnetic

anisotropy direction, as shown in Fig. 5(d). This results in significant magnetic hardening with  $H_C$  shooting up to 728 A/m, as indicated in Fig. 1.

The Kerr micrograph of the AQ ribbons suggests that the magnetic anisotropy is predominantly oriented perpendicular to the ribbon axis (the length of the ribbon), as shown in Fig. 6(a). However, in some regions, typically limited to 5%–10% of a 1.5 cm long ribbon segment, anisotropy aligns along the ribbon axis, as shown in Fig. 6(b–c). The origin of this anisotropy orientation in the AQ ribbon is the compressive stress that aligns the domains along the width of the ribbon through positive magnetostriction [13,29]. At optimal  $T_a$ , the stress inhomogeneity that causes maze-like domains due to a combination of perpendicular and in-plane magnetic anisotropy is relieved, resulting in wide domains, as shown in Fig. 6(d). After annealing above the optimal  $T_a$ , the crystallized surface layer, which is under tensile stress, exerts compressive stress in the amorphous bulk region of the sample, influencing the direction of magnetic moments [29]. Annealing at 400 °C does not alter the magnetic anisotropy orientation (Fig. 6(e)) compared to the AQ ribbon (Fig. 6(b)). At  $T_a = 435$  °C, as we reach near the supercooled liquid region (close to  $T_g = 440$  °C, as calculated from the DSC curve in Fig. 3) with an annealing time of 20 min, some crystallization is expected. Crystallization imposes compressive stress on the amorphous regions, causing the domains to align along the width of the ribbon through positive magnetostriction, as shown in Fig. 6(c) and (f). For better comparison, the pre-and post-annealing images are collected in the same ribbon region and with the same microscope settings, except for the Kerr sensitivity that is adjusted according to the magnetic anisotropy alignment, as indicated in Fig. 6.

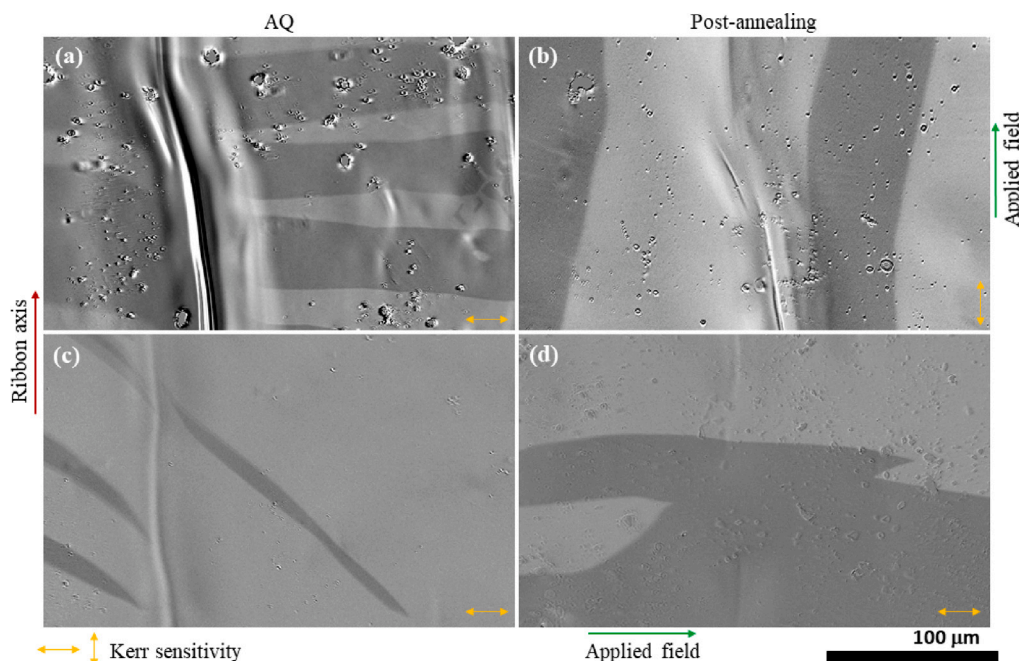


**Fig. 7.** Kerr microscopy images of (a), (c) AQ and field-annealed ribbons at 400 °C for  $t_a = 20$  min under (b) LFA and (d) TFA. The same ribbon region was imaged before and after annealing for each annealing condition. The applied field direction during annealing and the Kerr sensitivity while collecting the domain images are indicated in the respective image.

The effect of magnetic field annealing is studied on the BMG ribbons. Fig. 7 shows the change in domain alignment following magnetic-field-assisted annealing. Longitudinal field annealing (LFA) at 400 °C for  $t_a = 20$  min enables the magnetic anisotropy to reorient along the applied field direction. More interestingly, with LFA, there is no signature of crystallization, as confirmed by the magnetic measurements ( $H_C$  in Fig. 1), domain imaging, and XRD pattern (Figure S2). As shown in Fig. 7(b), LFA results in wider domains, fewer domain walls, and no pinning, compared to the AQ ribbon shown in Fig. 7(a), enabling low  $H_C = 15$  A/m. Similarly, under TFA at the same  $T_a$  and  $t_a$ , the magnetic domains become broader with fewer domain walls, as shown in Fig. 7(d), keeping the magnetic anisotropy orientation consistent with the pre-annealing state (Fig. 7(c)). Furthermore, TFA achieves the same reduction in coercivity to  $H_C = 15$  A/m, demonstrating the effectiveness of field annealing without inducing crystallization.

To further investigate the effect of field annealing on crystallization and domain switching at 400 °C, the annealing time was increased to 50 min. Fig. 8 presents the domain patterns of the different regions of the annealed ribbon. Evidence of cluster formation or surface crystallization is observed in Fig. 8(a). Notably, only 10% of the ribbon length exhibits domain patterns aligned along the ribbon axis (shown in Fig. 8(b)), while the rest display transverse domain patterns (Fig. 8(c)). Although the domain patterns are wide, some pinning effects are observed (marked in yellow in Fig. 8(c)). With this prolonged annealing,  $H_C$  decreases from 15 A/m (for  $t_a = 20$  min) to 13.5 A/m. This observation can be associated with magnetic softening, owing to the reduced number of domain walls with field-assisted annealing. The prolonged annealing time, however, is not suitable for reprogramming the magnetic anisotropy along  $H$  as it introduces local anisotropies in the BMG system likely as a result of cluster formation.

For a better understanding of the effect of the applied magnetic field on magnetic domain switching and crystallization in the temperature ranges where zero-field annealed ribbons show the crystallization signature,  $T_a$  was increased to 420 °C and 435 °C. The magnetic domains of the ribbons were imaged before and after annealing in the same region to understand the effect of annealing. At  $T_a = 420$  °C, the magnetic domains that were aligned along the ribbon axis in the AQ

system remain unchanged post-annealing, exhibiting broader domains, as shown in Fig. 9(a) and (b), for region 1 of the ribbon. However, this particular annealing condition proves unsuitable for reprogramming the transverse domain alignment under the influence of  $H$ . As shown in Fig. 9(c) and (d), for region 2, the magnetic anisotropy orientation remains unchanged between the pre- and post-annealing states. Only 5% of the ribbon regions exhibit switching of magnetic domains along applied  $H$ , as shown in Fig. 9(e) and (f). For LFA at 420 °C, no sign of crystallization is observed based on the XRD pattern,  $H_C$ , and domain imaging. The  $H_C$  value of the ribbons annealed at 420 °C remains the same as that annealed at 400 °C under LFA. Fig. 10 shows the effect of LFA at  $T_a = 435$  °C by comparing the domains of the AQ (Fig. 10(a)) and annealed (Fig. 10(b)) ribbons. Unlike at 420 °C, the signature of surface crystallization is prominent at 435 °C, with the formation of crisscross domain patterns along with wide transverse domains, as shown in Fig. 10(b). Moreover, a comparison of the pre- and post-annealed domains in Fig. 10(c) and (d) reveals switch of the domains from longitudinal to transverse orientation, even under the application of  $H$  along the ribbon axis during LFA, highlighting the dominant effect of crystallization for  $T_a = 435$  °C.

To elucidate the effect of the applied magnetic field on reprogramming magnetic anisotropy and crystallization, the Curie temperature ( $T_C$ ) of the amorphous phase has to be taken into account. As  $T_C$  is not very prominent from the DSC curve in Fig. 3, the temperature dependence of ac susceptibility  $\chi(T)$  (Fig. 11) is analyzed to obtain  $T_C$  of the AQ and the annealed samples. The experimental data were recorded during both the heating and cooling cycles as indicated in Fig. 11(a) and (b), respectively. The  $T_C$  of the amorphous phase (determined from the inflection point in Fig. 11(c)) of the AQ sample is  $\sim 416$  °C. When the AQ ribbons were annealed at  $T_a = 420$  °C, some of the transverse magnetic domains switched to the applied field direction as  $T_a \cong T_C$ . However, at  $T_a > T_C$  the system is in the paramagnetic state with a very weak effect of the applied  $H$  on the Fe atoms. A closer examination of the enlarged region of the  $\chi$  vs.  $T$  plot in Fig. 11(d) shows the high-temperature peaks corresponding to the first crystallization temperature  $T_{x1}$  of the bcc Fe phase for the respective samples. Table 1 provides a detailed list of  $T_C$  and  $T_{x1}$  for

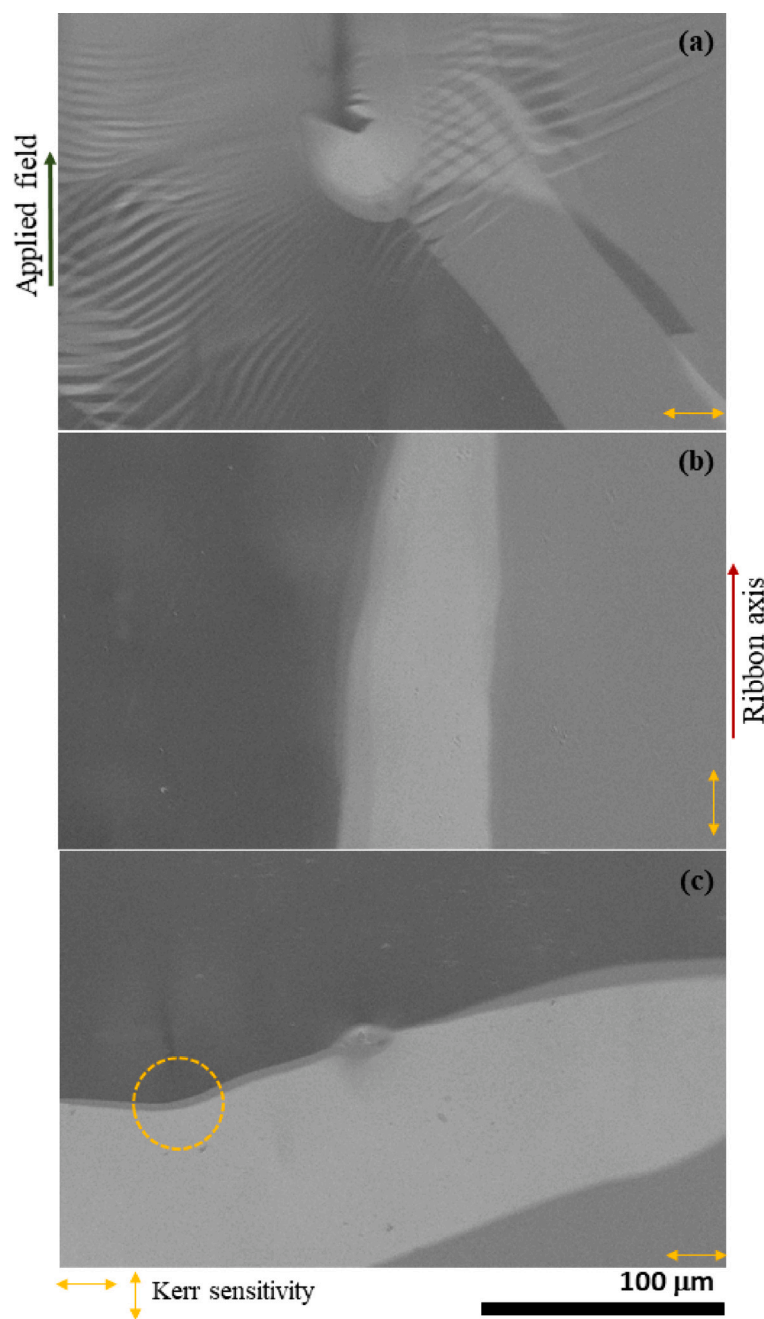


**Fig. 8.** (a–c) Magnetic domain pattern of the ribbon annealed under LFA at 400 °C for  $t_a = 50$  min. The applied field direction during annealing and the Kerr sensitivity while collecting the domain images are indicated in the figure. The pinning site is marked in a yellow circle in (c).

the AQ and the annealed samples. With LFA,  $T_{x1}$  shifts towards a lower temperature. This implies that crystal formation, both in LFA and in TFA, at  $T_a = 400$  °C could be avoided for  $t_a = 20$  min due to the obstacle to cluster formation between Fe atoms under  $H = 16$  kA/m, where the system is in the ferromagnetic state in the approach region to saturation with all magnetic moments aligned in the applied field direction. However, with  $t_a = 50$  min at the same  $T_a$ , the atoms form clusters or nanocrystals. On the other hand, an extended annealing time from 20 min to 50 min, in LFA at  $T_a = 400$  °C, enhances the magnetic softness with longer  $t_a$ , due to stress relaxation. As  $T_a$  approaches  $T_C$ , the difference between  $T_{x1}$  under field annealing and normal annealing diminishes. Interestingly, annealing the ribbons below the supercooled liquid region reduces  $T_{x1}$  and reduces further when annealed in the presence of  $H$ . However, when  $T_a$  approaches the supercooled liquid region, i.e., for  $T_a = 435$  °C in the presence or absence of  $H$ ,  $T_{x1}$

increases to that of the AQ state. This implies that annealing the ribbons in the supercooled liquid region causing a similar or equivalent stress and local pinning to those of the AQ state, originated from the clustering after annealing, resulting in equal  $T_{x1}$  and  $T_C$ . Notably,  $T_g$  and  $T_{x1}$  are dynamic variables and are affected by the magnetic field and the heating rate. For both the DSC and  $\chi$  vs.  $T$  measurements, the heating rate was kept the same at 10 °C/min.  $T_C$  of the crystalline phase can be determined from the cooling curve in Fig. 11(b). Taking into account that the  $T_C$  of  $\alpha$ -Fe is  $\sim 770$  °C, the peak in the cooling curve represent the  $T_C$  of another crystalline phase present in the system formed during the heating cycle. From the XRD pattern analysis of the ribbon annealed at 480 °C in Figure S2 of the supplementary material information, it is observed that along with the formation of  $\alpha$ -Fe as the most prominent crystalline phase, some phases are formed as the solid solution of Fe-Si and B-Fe-P. The  $\tau_1$  phase ( $\text{Fe}_3\text{B}_x\text{P}_{1-x}$ ) of the ternary

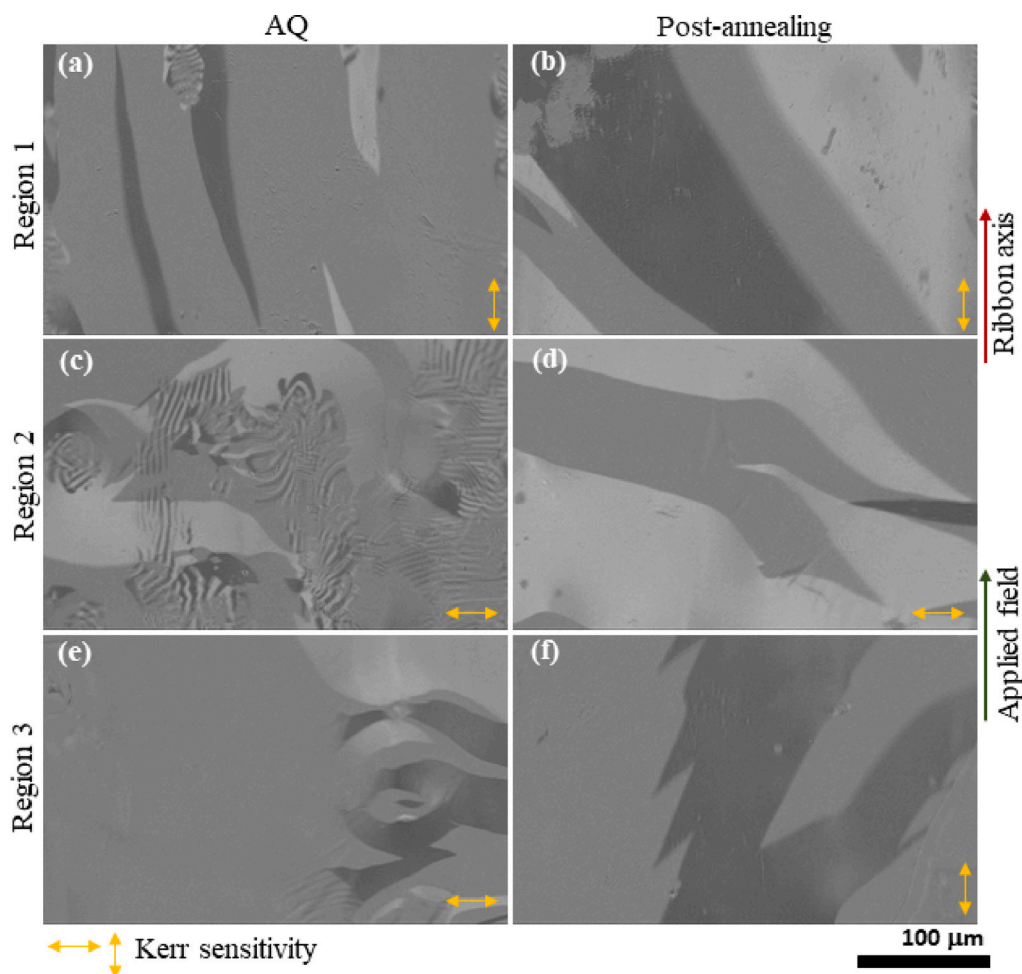


**Fig. 9.** MOKE micrographs of the (a), (c), (e) AQ and (b), (d), (f) ribbons annealed at 420 °C for  $t_a = 20$  min under LFA (applied  $H$  direction is shown). The Kerr sensitivity while collecting the domain images is indicated in the respective image. For better comparison, the same ribbon region was imaged before and after annealing.

**Table 1**

Variation of  $T_c$  of the amorphous and  $\tau_1$  crystalline phases and of  $T_{x1}$  with different annealing conditions ( $t_a = 20$  min).

$T_a$	$T_c$ (Amorphous phase)	$T_{x1}$	$T_c$ ( $\tau_1$ phase)
AQ	416 °C	515 °C	577 °C
400 °C	420 °C	509 °C	582 °C
LFA 400 °C	406 °C	501 °C	570 °C
LFA 420 °C	419 °C	507 °C	575 °C
435 °C	421 °C	515 °C	579 °C
LFA 435 °C	421 °C	513 °C	581 °C

B-Fe-P system forms a stable solid solution in the composition range  $0.5 < x < 1$  [30]. The  $T_C$  of the  $\text{Fe}_3\text{B}_{0.82}\text{P}_{0.18}$  ( $\tau_1$ ) composition is reported to be 527 °C [30].

The occurrence of a rapid increase in the susceptibility cooling curve around 580 °C should correspond to the  $T_C$  of the  $\tau_1$  phase of the ternary B-Fe-P system. We note that the observed higher value of  $T_C$  of the  $\tau_1$  phase is likely because of the possible presence of C and Si in the solid solution of B-Fe-P. The values of  $T_C$  of the crystalline  $\tau_1$  phase after different annealing conditions are included in Table 1.

During magnetic field-assisted annealing, the magnetic moments rotate along the applied field direction to maintain equilibrium between the torque imposed on them by local anisotropies and the

applied field [31]. Magnetostriction plays a crucial role in the domain-reorientation process under field-assisted annealing. In Fe-based amorphous systems with positive magnetostriction, the magnetoelastic coupling energetically favors domain alignment along the local tensile stress direction. During field annealing below  $T_C$ , a positive magnetostriction yields a slight expansion of the sample along the applied field direction. At a sufficiently high annealing temperature, where the amorphous system is in a stress-relieved state, the applied magnetic field and magnetostrictive strain influence the atomic rearrangement. Therefore, on cooling, a slightly different atomic arrangement is frozen in involving only short-range rearrangements of the atomic positions. If no other competing anisotropies exist (the sample is in a stress-relieved state without crystallites), the global anisotropy can be reprogrammed to this field-induced anisotropy. At  $T_a = 400$  °C,  $t_a = 20$  min, and  $H = 16$  kA/m, the field-induced anisotropy is sufficient to reorient the total magnetic anisotropy along the applied  $H$ . However, when crystallization-induced local anisotropy become significant, as when  $t_a$  is increased to 50 min, these competing local anisotropies are stronger. Therefore, only some domains are aligned along the ribbon axis, i.e., along the applied  $H$ . Magnetostriction actively supports anisotropy reprogramming by locking in the new atomic arrangement along the applied field direction under suitable annealing conditions, predominantly when the system is in a ferromagnetic, amorphous, and stress-relieved state.

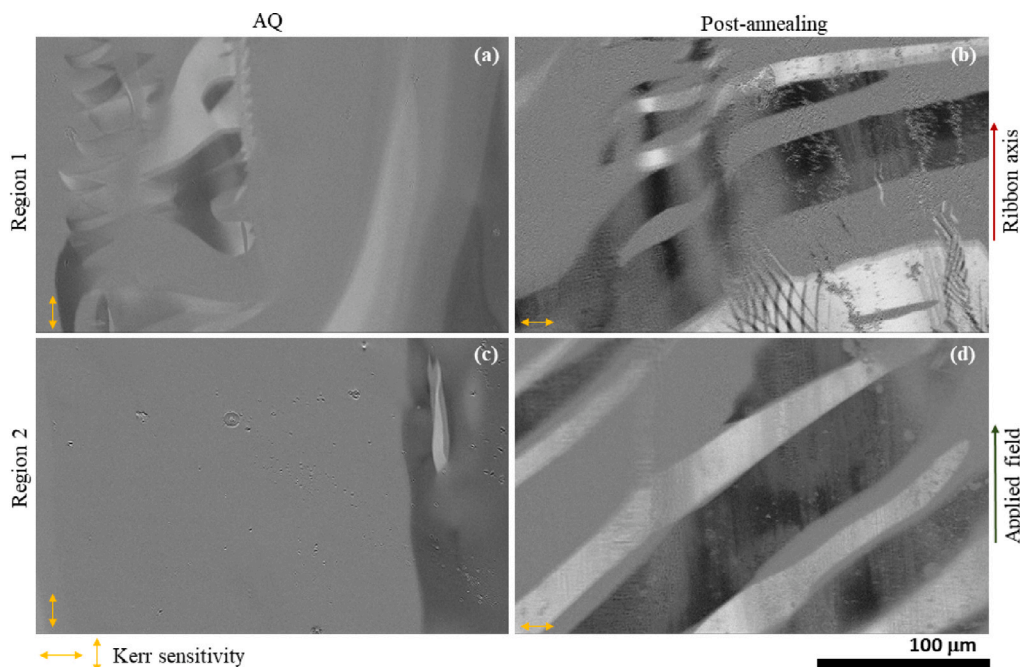


**Fig. 10.** Domain images of AQ and LFA 435 °C ribbons annealed for  $t_a = 20$  min. (a) AQ and (b) post-annealing in Region 1, and (c) AQ and (d) annealed domain pattern in Region 2. For better comparison, the domain images are collected in the same ribbon regions before and after annealing. The Kerr sensitivity while collecting the domain images is indicated in the respective image.

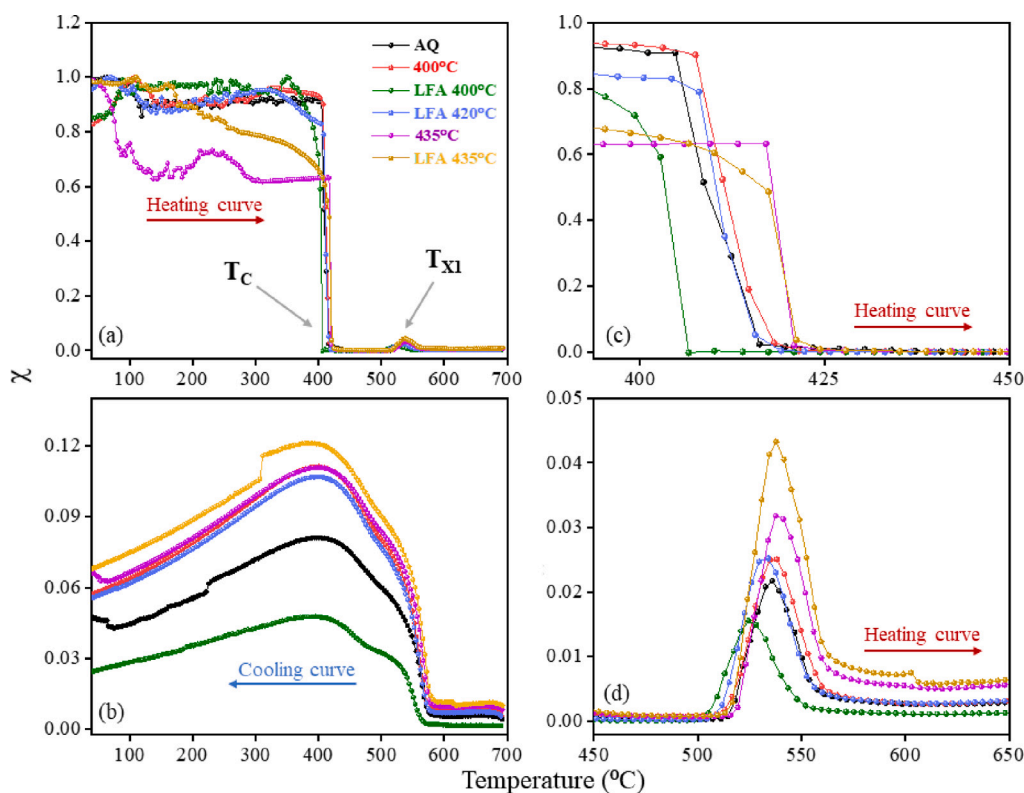


**Fig. 11.** Susceptibility vs temperature plots for the AQ and annealed samples ( $t_a = 20$  min) during the (a) heating and (b) cooling cycles. The enlarged regions of the heating curve for proper interpretation of (c) the  $T_C$  of the amorphous phase and (d)  $T_{X1}$ .

At  $T_a = 420$  °C under LFA, there is no crystallization-induced domain switching, as evident in Fig. 9(a) and (b). Additionally, as  $T_a \sim T_C$  only 5% of the total measuring window shows field-induced domain switching under this annealing condition. For a more comprehensive interpretation, examining the domain patterns under different Kerr

sensitivities, i.e., longitudinal and transverse modes, provides a better understanding of the magnetic anisotropy orientation in the pre- and post-annealed states. Figure S4 in the supplementary material information highlights two different regions of the ribbon annealed at 420 °C under LFA. It is observed that in the annealed ribbon, the longitudinal

Kerr sensitivity dominates over the transverse sensitivity. At 435 °C under LFA, however, the crystallization-induced domain switching is evident from Fig. 10(c) and (d). A comparison of the domain patterns in Figures 6(c) and (f) with those in Figures 10(c) and (d) suggests that the presence of an applied field during annealing at  $T > T_C$  does not influence the process. This observation is further supported by the identical values of  $H_C$  (Fig. 1(b)) and  $T_{X1}$  (Fig. 11(d)) for ribbons annealed at 435 °C, both with and without an applied magnetic field.

With zero field annealing,  $T_{X1}$  shifts towards a lower temperature when  $T_a < T_g$ . At the same  $T_a$  and  $t_a$ , the presence of a magnetic field reduces  $T_{X1}$  further down compared to the zero field condition. However, we can achieve reprogrammed magnetic anisotropy in these BMGs at  $T_a = 400$  °C without crystallizing the amorphous system due to the magnetic field-assisted atomic arrangement of Fe atoms. Reprogramming of magnetic domains by field-assisted annealing is achievable below  $T_C$  only when the amorphous system is stress-relieved. Magnetostriction governs the anisotropy reprogramming process. For  $T_a$  above  $T_C$ , field annealing is not efficient in reprogramming magnetic anisotropy with  $H = 16$  kA/m since local anisotropies occurred due to crystallization or cluster formation. The influence of field annealing on P-containing Fe-rich BMGs, particularly regarding thermally induced surface versus bulk cluster formation, remains an open question and can be addressed further through in situ structural and magnetic characterization.

#### 4. Conclusion

In summary, this study provides valuable insights into the stress signatures and evolution of magnetic anisotropy in rapidly quenched  $\text{Fe}_{80}\text{B}_{12}\text{P}_4\text{Si}_{2.7}\text{C}_{1.3}$  ribbons subjected to heat treatment in the presence and absence of a magnetic field. Kerr microscopy imaging, combined with magnetic measurements, reveals a clear transition from maze-like to wide-domain structures as the annealing temperature increases, driven by stress relaxation. The results highlight the sensitivity of crystallization to annealing conditions, where magnetic field-assisted annealing successfully inhibits crystallization while reprogramming magnetic anisotropy along the applied field direction. A key finding is that optimal field annealing with  $H = 16$  kA/m below  $T_C$  at 400 °C for  $t_a = 20$  min effectively reprograms magnetic anisotropy without triggering crystallization. Our finding reveals that reprogramming of magnetic domains is effective when the annealing temperature is high enough to stress relieve the amorphous system, but still below its Curie temperature and well below the crystallization temperature. The anisotropy reprogramming is achieved through the magnetic-field-induced tensile stress due to magnetostriction. Prolonged annealing or high processing temperatures lead to crystallization-induced anisotropies, which introduces random local anisotropies stronger than the field-induced anisotropy. These findings contribute to a deeper understanding of field-assisted stress relaxation in Fe-based BMGs and provide a pathway for optimizing their magnetic performance for high-efficiency applications.

#### CRediT authorship contribution statement

**Priyanka Saha:** Writing – review & editing, Writing – original draft, Visualization, Validation, Project administration, Methodology, Investigation, Formal analysis, Conceptualization. **Julia Löfstrand:** Writing – review & editing, Investigation. **Fernando Maccari:** Investigation. **Franziska Scheibel:** Writing – review & editing, Investigation. **Oliver Gutfleisch:** Writing – review & editing, Resources. **Martin Sahlberg:** Writing – review & editing, Resources. **Petra E. Jönsson:** Writing – review & editing, Validation, Supervision, Resources, Project administration, Funding acquisition, Conceptualization.

#### Declaration of competing interest

The authors declare that they have no known competing financial interests or personal relationships that could have appeared to influence the work reported in this article.

#### Acknowledgments

This research was supported by the Carl Trygger Foundation, Sweden (Project No. 113601127) and the Swedish Energy Agency, Sweden (research project grant P48716-1). The authors from TU Darmstadt acknowledge financial support from the Deutsche Forschungsgemeinschaft (DFG), Germany within the CRC/TRR 270 collaborative research center (Project-ID 405553726). We also acknowledge Anna Maria Lundins Stipendiefond for awarding a travel grant that enabled J. Löfstrand's research exchange at TU Darmstadt. We are grateful to Bjarne Almqvist for his assistance with the temperature-dependent AC susceptibility measurements, conducted at the Department of Earth Sciences, Geophysics, Uppsala University.

#### Appendix A. Supplementary data

Supplementary material related to this article can be found online at <https://doi.org/10.1016/j.jallcom.2025.183153>.

#### References

- [1] J.M. Silveyra, E. Ferrara, D.L. Huber, T.C. Monson, Soft magnetic materials for a sustainable and electrified world, *Science* 362 (6413) (2018) eaa0195.
- [2] O. Gutfleisch, M.A. Willard, E. Brück, C.H. Chen, S. Sankar, J.P. Liu, Magnetic materials and devices for the 21st century: stronger, lighter, and more energy efficient, *Adv. Mater.* 23 (7) (2011) 821–842.
- [3] R. Parsons, K. Suzuki, Nanocrystalline soft magnetic materials produced by continuous ultra-rapid annealing (cura), *AIP Adv.* 12 (3) (2022).
- [4] P. Murugaiyan, A. Mitra, A.K. Patro, R.K. Roy, M. Churyukanova, S. Kaloshkin, E. Shuvaeva, A.K. Panda, Role of p on amorphization, microstructure, thermo-physical and soft magnetic properties of Fe-rich FeB(P)SiNbCu melt-spun alloys, *J. Magn. Magn. Mater.* 492 (2019) 165723.
- [5] Y. Ogawa, M. Naoe, Y. Yoshizawa, R. Hasegawa, Magnetic properties of high Bs Fe-based amorphous material, *J. Magn. Magn. Mater.* 304 (2) (2006) e675–e677.
- [6] V. Zhukova, O. Korchuganova, A. Aleev, V. Tcherdyntsev, M. Churyukanova, E. Medvedeva, S. Seils, J. Wagner, M. Ipatov, J. Blanco, et al., Effect of annealing on magnetic properties and structure of Fe-Ni based magnetic microwires, *J. Magn. Magn. Mater.* 433 (2017) 278–284.
- [7] H. Li, A. He, A. Wang, L. Xie, Q. Li, C. Zhao, G. Zhang, P. Chen, Improvement of soft magnetic properties for distinctly high Fe content amorphous alloys via longitudinal magnetic field annealing, *J. Magn. Magn. Mater.* 471 (2019) 110–115.
- [8] N. Bruno, N. Adoo, E. Meakins, V. Keylin, G. Feichter, R. Noebe, The effect of stress-annealing on the mechanical and magnetic properties of several Fe-based metal-amorphous nano-composite soft magnetic alloys, *J. Non-Cryst. Solids* 600 (2023) 122037.
- [9] A. Makino, H. Men, T. Kubota, K. Yubuta, A. Inoue, New excellent soft magnetic Fe-based amorphous alloys with high Bs of 1.9T from nanohetero-amorphous phase, *IEEE Trans. Magn.* 45 (10) (2009) 4302–4305.
- [10] L. Shi, K. Yao, Composition design for Fe-based soft magnetic amorphous and nanocrystalline alloys with high Fe content, *Mater. Des.* 189 (2020) 108511.
- [11] A. Wang, C. Zhao, A. He, H. Men, C. Chang, X. Wang, Composition design of high Bs Fe-based amorphous alloys with good amorphous-forming ability, *J. Alloys Compd.* 656 (2016) 729–734.
- [12] B. Butvinová, P. Butvin, K. Brzózka, M. Kuzminski, I. Mat'ko, P. Švec Sr, M. Chromčíková, Effects of surface crystallization and oxidation in nanocrystalline FeNbCuSiB(P) ribbons, *J. Magn. Magn. Mater.* 424 (2017) 233–237.
- [13] E. Lopatina, I. Soldatov, V. Budinsky, M. Marsilius, L. Schultz, G. Herzer, R. Schäfer, Surface crystallization and magnetic properties of Fe84.3Cu0.7Si4b8p3 soft magnetic ribbons, *Acta Mater.* 96 (2015) 10–17.
- [14] U. Köster, Surface crystallization of metallic glasses, *Mater. Sci. Eng.* 97 (1988) 233–239.
- [15] P. Ohodnicki, J. Egbu, Y. Yu, J. Baltrus, N. Aronhime, Y. Krimer, P. Anand, K. Byerly, M. McHenry, Surface oxidation and crystallization of FeNi-based soft magnetic nanocrystalline and amorphous nanocomposite alloys, *J. Alloys Compd.* 834 (2020) 155038.
- [16] C. Minnert, M. Kuhnt, S. Bruns, A. Marshal, K.G. Pradeep, M. Marsilius, E. Bruder, K. Durst, Study on the embrittlement of flash annealed Fe85.2b9.5p4cu0.8si0.5 metallic glass ribbons, *Mater. Des.* 156 (2018) 252–261, <http://dx.doi.org/10.1016/j.matdes.2018.06.055>.
- [17] W. Kim, T. Duan, J.H. Perepezko, Nanocrystal evolution during ultra-fast heating in an amorphous Fe85b15 alloy, *Scr. Mater.* 225 (2023) 115155.
- [18] K. Suzuki, N. Ito, S. Saranu, U. Herr, A. Michels, J.S. Garitaonandia, Magnetic domains and annealing-induced magnetic anisotropy in nanocrystalline soft magnetic materials, *J. Appl. Phys.* 103 (7) (2008).

- [19] C. Zhao, A. Wang, S. Yue, T. Liu, A. He, C. Chang, X. Wang, C.-T. Liu, Significant improvement of soft magnetic properties for Fe(Co)BPSiC amorphous alloys by magnetic field annealing, *J. Alloys Compd.* 742 (2018) 220–225.
- [20] V. Procházka, V. Vrba, D. Smrčka, R. Růffer, P. Matúš, M. Mašláň, M. Miglierini, Structural transformation of nanoperm-type metallic glasses followed in situ by synchrotron radiation during thermal annealing in external magnetic field, *J. Alloys Compd.* 638 (2015) 398–404.
- [21] P. Marin, A. Hernando, Enhanced magnetic properties of FeCo ribbons nanocrystallized in magnetic field, *Appl. Phys. Lett.* 94 (12) (2009).
- [22] C. Wang, Z. Wu, X. Feng, Z. Li, Y. Gu, Y. Zhang, X. Tan, H. Xu, The effects of magnetic field annealing on the magnetic properties and microstructure of Fe<sub>80</sub>Si<sub>9</sub>B<sub>11</sub> amorphous alloys, *Intermetallics* 118 (2020) 106689.
- [23] M. Miglierini, V. Procházka, R. Růffer, R. Zbořil, In situ crystallization of metallic glasses during magnetic field annealing, *Acta Mater.* 91 (2015) 50–56.
- [24] M. Chen, A brief overview of bulk metallic glasses, *NPG Asia Mater.* 3 (9) (2011) 82–90.
- [25] Z. Hussain, S.H. Babu, V.R. Reddy, Appearance of inverted hysteresis, pinning effect in amorphous FeCoB ribbon with annealing: A Kerr microscopy investigation, *J. Non-Cryst. Solids* 571 (2021) 121073.
- [26] Z. Tang, R. Parsons, K. Suzuki, Effect of metalloid additives on the effectiveness of ultra-rapid annealing in Fe-B based nanocrystalline alloys, *J. Magn. Magn. Mater.* 592 (2024) 171812.
- [27] K. Suzuki, J. Cadogan, Random magnetocrystalline anisotropy in two-phase nanocrystalline systems, *Phys. Rev. B* 58 (5) (1998) 2730.
- [28] R. Schäfer, A. Hubert, G. Herzer, Domain observation on nanocrystalline material, *J. Appl. Phys.* 69 (8) (1991) 5325–5327.
- [29] H.N. Ok, A. Morrish, Origin of the perpendicular anisotropy in amorphous Fe<sub>82</sub>B<sub>12</sub>Si<sub>6</sub> ribbons, *Phys. Rev. B* 23 (5) (1981) 2257.
- [30] W. Martienssen G. Effenberg (Ed.), *Iron Systems, Part 4: Selected Systems from Cu-Fe-Si To Fe-N-U*, 11D4 of Landolt-Börnstein - Group IV Physical Chemistry, Springer Berlin Heidelberg, Berlin, Heidelberg, 2008.
- [31] C. Appino, C. Beatrice, E. Ferrara, F. Fiorillo, et al., Magnetization process and magnetic losses in field-annealed amorphous and nanocrystalline ribbons, *J. Optoelectron. Adv. Mater.* 6 (2004) 511–522.